Nano Energy 143 (2025) 111316

Contents lists available at ScienceDirect

Nano Energy

journal homepage: www.elsevier.com/locate/nanoen

Full paper

Highly efficient large-area quantum dot near-infrared light-emitting device for advanced non-invasive bioimaging

Nasrud Din [a], Fawad Saeed [a], Sajid Hussain [a], Rai Muhammad Dawood Sultan [a], Zhang Yuyi [a], Premkumar Sellan [a], Qing Li [a], Zhiwei Zhao [a], Zhuoya Zhu [a], Jianming Zhou [b], Byung Seong Bae [c], Damian C. Onwudiwe [d], Qasim Khan [a,e,*], Zaman Ashraf [f,**], Wei Lei [a,**]

[a] Joint International Laboratory of Information Display and Visualization, School of Electronic Science and Engineering, Southeast University, Nanjing 210096, China
[b] E-xray Electronic Co. Ltd., Suzhou 215131, China
[c] Department of Electronics & Display Engineering Hoseo University, Hoseo Ro 79, Asan, Chungnam 31499, Republic of Korea
[d] Department of Chemistry, School of Mathematics and Physical Sciences, Faculty of Natural and Agricultural Sciences North-West University Mafikeng Campus, Private Bag X2046, Mmabatho 2735, South Africa
[e] Schulich School of Engineering, University of Calgary, Calgary, AB T2N 1N4, Canada
[f] Department of Chemistry, Rawalpindi Women University, Rawalpindi 46300 Pakistan

ARTICLE INFO

Keywords:
NIR-QLED
Larger-area devices
Non-invasive bioimaging
Radiance
Industrial-friendly

ABSTRACT

Advanced bioimaging requires a uniform and large-area near-infrared (NIR) light illumination source. Achieving uniform light typically involves the use of inorganic near-infrared light-emitting diodes (NIR-LEDs), such as AlGaAs or GaAs, which are often complemented by additional optical components like reflectors and diffusers. However, the use of such optical components imposes limitations on their applicability and flexibility. On the other hand, Quantum dot NIR LEDs (NIR-QLEDs) offer distinct advantages for bioimaging, as they directly emit light uniformly across their entire surface, without the need for any additional optical components. However, for state-of-the-art quantum dot-based NIR LEDs, the previous NIR-QLEDs have suffered from suboptimal charge transport and rapid degradation, limiting their radiance and EQE. This work addresses these limitations by demonstrating an industrial-friendly, all-solution processing technique for NIR-QLED device fabrication with significantly enhanced radiance and efficiency by utilizing copper (Cu) doped InP/ZnSe quantum dots (QDs). Cu-doping in InP/ZnSe QDs generates localized intra-gap states, enhancing carrier trapping and radiative recombination while suppressing non-radiative pathways, leading to unprecedented NIR peak emission at 924 nm and a narrow full-width at half maximum (FWHM) of 81 nm. These intra-gap states facilitate pure NIR emission, thereby substantially enhancing the device's efficiency. Based on the energy levels of the doped InP/ZnSe quantum dots (QDs), ZnMgO and WO_3 are employed as the electron transport layer (ETL) and hole transport layer (HTL), respectively. ZnMgO and WO_3 provide favorable conduction and valence band offsets, ensuring efficient carrier injection while suppressing leakage currents. The NIR-QLED exhibited an external quantum efficiency (EQE) of approximately 16 %. With a high current density of 250×10^{-3} A cm^{-2}, the radiance improved to 62 W sr^{-1} m^{-2}. The all-solution processing technique employed in this work enabled the fabrication of a large emission area measuring 35 mm × 35 mm. Under illumination from this NIR-QLED, subcutaneous deep vein images were clearly observable. Consequently, this all-solution process not only simplifies the production process but also facilitates scalability, paving the robust route for the development of larger-area devices tailored for complex bioimaging applications.

* Corresponding author at: Joint International Laboratory of Information Display and Visualization, School of Electronic Science and Engineering, Southeast University, Nanjing 210096, China.
** Corresponding authors.
E-mail addresses: Qasim.khan@ucalgary.ca (Q. Khan), zaman.ashraf@f.rwu.edu.pk (Z. Ashraf), lw@seu.edu.cn (W. Lei).

https://doi.org/10.1016/j.nanoen.2025.111316
Received 16 April 2025; Received in revised form 22 June 2025; Accepted 8 July 2025
Available online 16 July 2025

1. Introduction

Near-infrared light-emitting diodes (NIR-LED) have widespread applications in remote sensing, security, optical communication, and biomedical imaging [1]. The Near-Infrared (NIR) wavelength range, 800–2500 nm, is highly versatile, with its wavelength of interest depending on the specific application [2]. In the field of in vivo bioimaging, NIR is particularly promising for visual examination, biological detection, and photodynamic therapy. Specific NIR wavelengths penetrate biological tissues due to reduced scattering and absorption, enabling deeper imaging. This property makes NIR an ideal tool for imaging and therapeutic applications in living organisms [3,4]. Typical NIR-LEDs are manufactured by a highly complex process that includes photolithography, molecular beam epitaxy (MBE), and metalorganic chemical vapor deposition (MOCVD) [5]. These complex and costly epitaxial growth techniques are employed to deposit III–V inorganic semiconductors, such as GaAs, InGaAs, and InGaAlAs [1,6–8]. Therefore, there is increasing demand for alternative fabrication techniques, making the development of innovative NIR LEDs increasingly crucial [9,10]. Compared to conventional NIR-LEDs, near-infrared quantum dot LEDs (NIR-QLEDs) offer a high alternative for surface lighting applications due to the unique properties of colloidal quantum dots (QDs). Unlike bulk semiconductors with fixed bandgaps, QDs exhibit size-dependent tunable emission due to quantum confinement effects. Additionally, QDs provide high colour purity, solution processability, and enhanced flexibility in device integration, distinguishing them from both bulk and molecular materials. These advantages make QDs an attractive candidate for next-generation NIR light sources with tailored optical and electronic properties [11,12].

Interestingly, the existing advancements primarily concentrate on cadmium-based QLEDs exhibit red and green efficiencies exceeding 25 %, while blue QLEDs surpass 20 % EQE [13]. However, the innate toxicity associated with cadmium-containing quantum dots (QDs) poses a major barrier to their widespread industrial use. Because of this problem, there has been a lot of interest in using cadmium-free materials including silicon, InP, ZnSe, and $CuInS_2$ to improve the performance of QLED devices. Si QDs often suffer from broad emission bandwidths, surface-related non-radiative pathways, and relatively low EQE, limiting their deployment in high-performance optoelectronic devices [14,15]. Among the several types of quantum dots (QDs), indium phosphide (InP) QDs are particularly noteworthy due to its remarkable ability to tune its color across a wide range of the solar spectrum and its exceptional emission properties. Consequently, InP QDs have emerged as a potential substitute for cadmium-based QDs in the development of efficient quantum dot light-emitting diodes (QLEDs) [16]. The production and optimization of indium phosphide quantum dots (InP QDs) have received a great deal of attention to improve the efficiency of quantum light-emitting diodes (QLEDs) [17].

PbSe QDs, synthesized via solution-based methods, demonstrate narrow, bright, and tunable NIR emissions [18]. PbSe QDs exhibit a pronounced ability for strong quantum confinement, as evidenced by a significant blue shift in absorption peaks with decreasing nanocrystal size [19]. This is explained by the significant exciton Bohr radius of 46 nm, which is about eight times larger than that of CdSe. Moreover, PbSe QDs exhibit an exceptionally high quantum yield, reaching up to 89 % in the near-to-mid infrared wavelength range, making them highly appealing as fluorophores for NIR LEDs [20]. But the external quantum efficiency (EQE), the ratio of emitted photons to the electrons injected, was not significantly improved [21]. To overcome this, Hu *et al.*, for instance, presented a ligand replacement method for PbSe QDs, although the device fabricated had an EQE of only 0.73 % [22]. Recently, another group achieved an EQE of 2 % by fabricating NIR LEDs using PbS QDs with ZnO as the charge transport layer [23–26]. Additionally, the Bulovic group reported an improved device performance by utilizing PbS/CdS core/shell QDs and achieved significantly increased EQE 4.3 % by adding the CdS shell, compared to devices that utilized core-only PbS QDs. Although lead chalcogenide QDs have been widely explored for NIR-LEDs, their EQE remains low due to several intrinsic limitations. These include high surface trap densities leading to non-radiative recombination, weak quantum confinement effects, strong Auger recombination, and poor charge injection efficiency [12,27–29]. To address these limitations, numerous efforts have been made to develop advanced NIR LEDs. Significant progress has been made, particularly in NIR LEDs with peak emissions categorized as NIR Ia (800–900 nm), NIR Ib (900–1000 nm), and NIR II (1000–1700 nm). However, despite the use of organic semiconductors and colloidal QDs, these devices continue to face major challenges, including poor operational stability and limited radiance, which hinder their practical applications [30]. Therefore, the development of novel materials is essential to fabricate efficient NIR-QLEDs for real-world use.

In this work, we have successfully synthesized environmentally sustainable InP/ZnSe core/shell QD doped with copper (Cu) to achieve tunable characteristics. The results indicate that the introduction of Cu doping into the InP/ZnSe induces a photoluminescence (PL) shift from the visible to the near-infrared (NIR) range, with the PL peak shifting from 650 nm to 924 nm. Moreover, the NIR LED based on these QDs demonstrated efficient charge transfer within the device. The incorporation of Cu as a dopant significantly enhanced the device's performance, yielding NIR emission centered at 924 nm with an FWHM of 81 nm. The device exhibited a relatively low turn-on voltage of 1.8 V, indicating efficient electron-hole recombination. As a result, a high EQE of 16 % was achieved, along with a peak radiance of 62 W sr^{-1} m^{-2}. These results underscore the potential of Cu doping in the InP/ZnSe QDs to improve their optoelectronic characteristics, enabling the development of highly efficient and stable NIR-QLEDs. This advancement holds promise for revolutionizing biological imaging technologies in the near future.

2. Results and discussion

2.1. Core/shell quantum dots with copper doping

Fig. 1 illustrates a schematic diagram of the synthesis process of InP/ZnSe:Cu QDs. The synthesis of copper-doped InP/ZnSe was achieved via a continuous thermal injection technique. Transmission electron microscopy (TEM) analysis, depicted in Fig. 2a, The HRTEM image confirms the formation of spherical InP/ZnSe:Cu QDs with an average size of ~7 nm. The inset highlights well-defined lattice fringes with an interplanar spacing of 0.4 nm. The clear fringes indicate high crystallinity, essential for efficient charge carrier transport and reduced non-radiative recombination. However, some degree of aggregation is observed, which may influence energy transfer processes. Notably, the structure integrity of the QDs demonstrates excellent reproducibility, as shown in the histogram in Fig. 2b, which shows a mean particle (QD) size of 7 ± 1.2 nm. The resultant InP/ZnSe:Cu QDs film, prepared via the antisolvent deposition technique, demonstrates an exceptionally low root mean square (RMS) roughness of ~ 0.9 nm (see Figure S2a Supporting Information). Cross-sectional SEM image of the fabricated NIR QLED structure as (see Figure S2b Supporting Information). The device shows a clear multilayer configuration consisting of a WO_3 hole transport layer (HTL), a Cu-doped InP/ZnSe quantum dot (QDs) emissive layer, and a ZnMgO electron transport layer (ETL). The image confirms uniform film formation and sharp interfacial layering, consistent with the intended device architecture.

The XRD spectrum in Fig. 2c exhibits diffraction peaks that match the cubic zinc blend structure of InP/ZnSe. The broad peak width indicates a nanoscale crystallite size consistent with the HRTEM observations. A slight peak shift relative to bulk InP/ZnSe suggests successful Cu incorporation, inducing lattice strain and potential modifications in the electronic structure. Energy-dispersive X-ray spectroscopy (EDAX) spectra of InP, InP/ZnSe and InP/ZnSe:Cu QDs, shown in Fig. 2d, clearly display the characteristic elemental peaks for each compound which

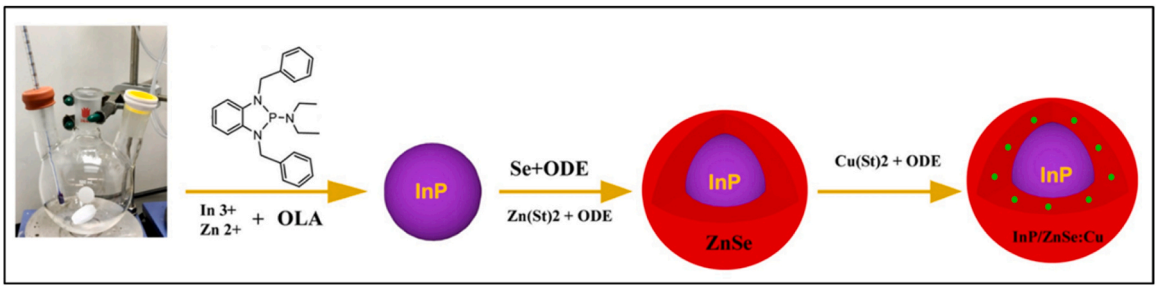

Fig. 1. Schematics of the InP/ZnSe: Cu QDs synthesis procedure.

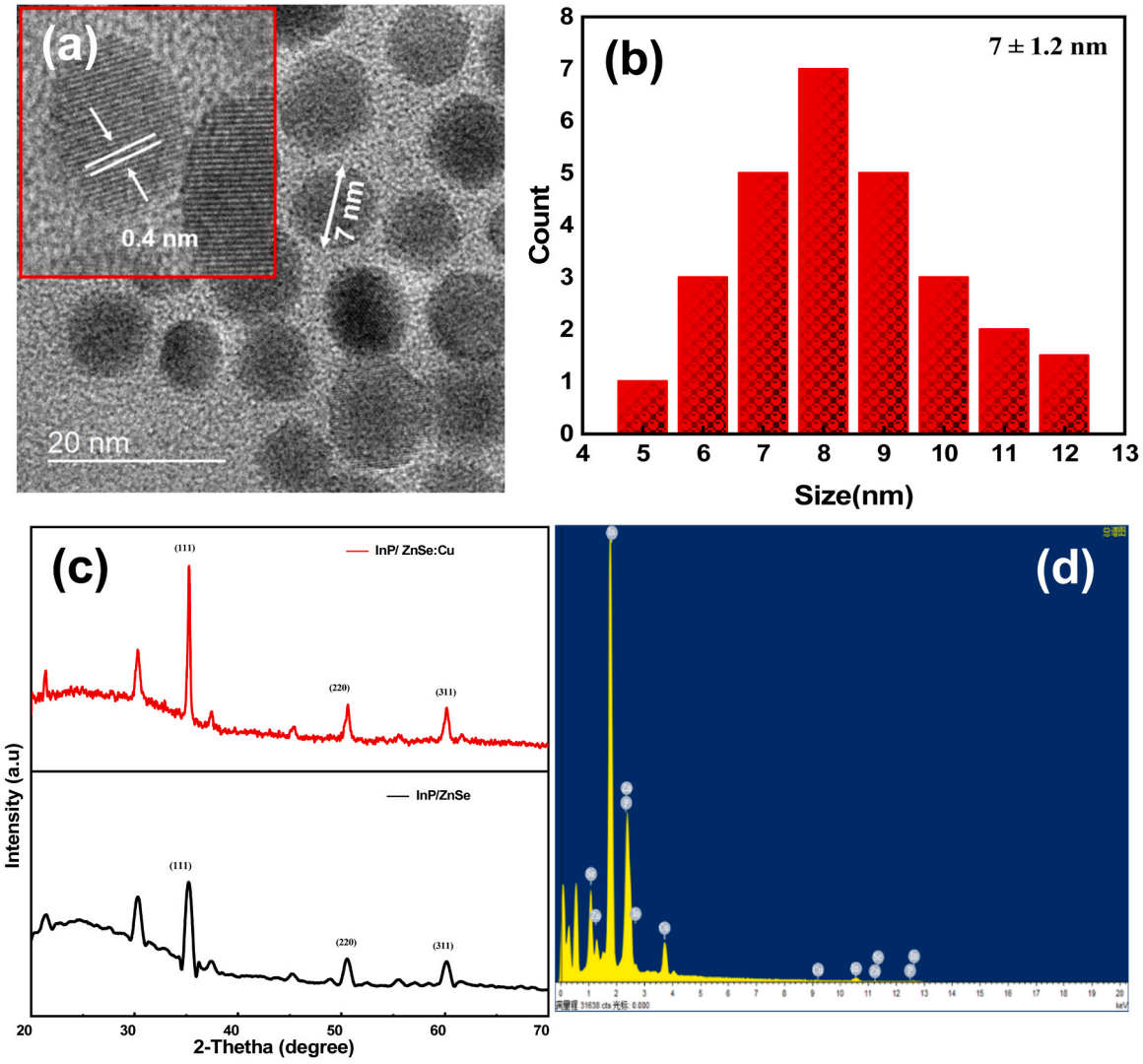

Fig. 2. **(a)** TEM image with HR-TEM, the inset showing the QD crystal, **(b)** Histogram peaks of QDs, **(c)** XRD Pattern of InP/ZnSe:Cu and **(d)** EDAX Pattern of InP/ZnSe:Cu.

confirms the successful synthesis of InP/ZnSe QDs, with distinct peaks corresponding to In, P, Zn, and Se. The detected Cu signal in Fig. 2d confirms successful doping, which may influence the electronic and optical properties of the QDs through defect states and altered band alignments.

The photoluminance spectra of InP/ZnSe and InP/ZnSe:Cu QDs are centered at 640 nm and 924 nm, respectively, as illustrated in Fig. 3a and 3b. The mild dual-shoulder absorption observed in Fig. 3a aligns with known behavior in InP/ZnSe core/shell quantum dots exhibiting slight size or compositional heterogeneity. Such inhomogeneity, particularly in core/shell systems, can lead to overlapping electronic transitions due to variations in shell growth and interface quality [31–33]. Furthermore, the emission spectrum exhibits a narrow bandwidth, characterised by a minimal full-width half-maximum (FWHM) value of 44 nm for undoped and 81 nm FWHM for Cu doped QDs. Fig. 3c shows the Raw photoluminescence (PL) spectra of InP/ZnSe QDs (black) and Cu-doped InP/ZnSe:Cu QDs (red), measured under identical conditions. The Cu-doped QDs exhibit a significantly higher PL intensity,

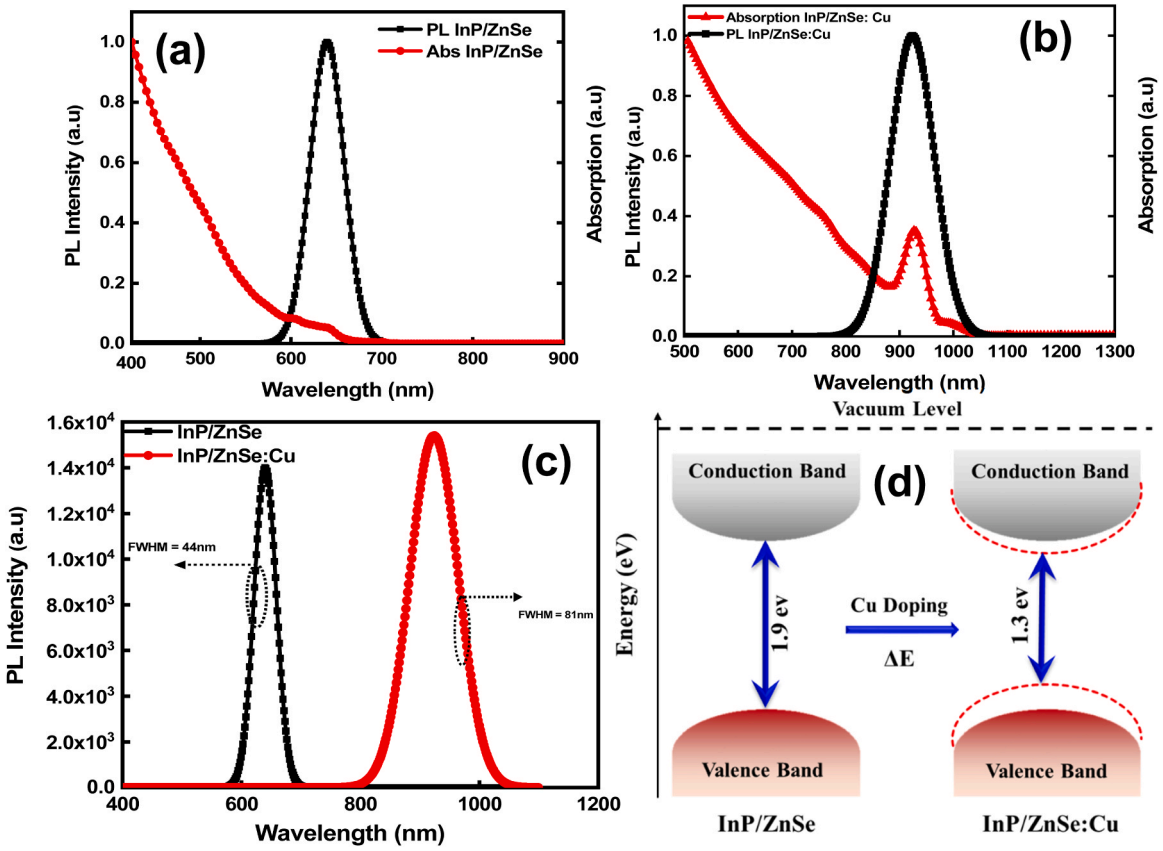

Fig. 3. Absorption and PL of **(a)** un-doped InP/ZnSe QDs and **(b)** doped InP/ZnSe:Cu QDs, Raw PL intensity of doped and undoped QDs **(d)** band gap of doped and undoped InP/ZnSe QDs.

confirming the enhancement effect of Cu doping. This enhancement is attributed to the reduction of surface trap states and the introduction of shallow acceptor states, promoting efficient radiative recombination. The film-based photoluminescent quantum yield (PLQY) was measured to be 30 %. For high-resolution biological imaging, the FWHM is a critical parameter influencing image quality and precision. A narrow FWHM is essential for bio-imaging applications as it ensures that the emitted light is confined within a specific wavelength range, enhancing spectral purity and contrast throughout the imaging process. This precision is essential for distinguishing between distinct biological tissues or molecular indicators by minimizing the overlap between the emission spectra of several fluorophores or light sources. The PL spectra depicted in Fig. 3b exhibit a narrow FWHM of approximately 81 nm, with a notable increase following Cu doping. This broadening of the FWHM is attributed to the increase in defect density states resulting in the emission peak's broadening. The addition of Cu atoms localizes the bandgap, thereby increasing the range of energies available for electron recombination and expanding the emission spectrum. The narrow FWHM enhances pseudo-colour precision and separation, enabling more vivid and realistic images by allowing more precise light localization [28]. To investigate the effect of Cu doping on the optical properties of InP/ZnSe QDs, QDs were synthesized with varying Cu concentrations (0.1 mL, 0.2 mL, and 0.3 mL). As shown in Figures S3a and S3b, both the PL peak wavelength and emission intensity exhibited a dependence on Cu doping levels. This suggests that Cu incorporation modulates the electronic structure of the QDs, influencing bandgap transitions and defect state interactions, thereby altering their optical characteristics. By varying the amount of Cu doping, the PL intensity of In/ZnSe QDs has significantly changed. The InP/ZnSe:(Cu-0.2 mL) QDs exhibited a significantly higher PL intensity compared to InP/ZnSe:(Cu-0.1 mL) QDs as (see Figure S3a Supporting Information). However, for InP/ZnSe:(Cu-0.3 mL) QDs, the excessive Cu doping created hole scattering centers, limiting the effective photoexcited electron transfer process, thereby reducing PL intensity [34].

Furthermore, the incorporation of Cu dopants modulates the electronic structure through two primary mechanisms. Firstly, Cu doping induces a bandgap reduction, as evidenced by the redshift in the absorption spectra (Fig. 3b). Secondly, it introduces mid-gap states that function as recombination centers, thereby enhancing PL emission in the NIR region. This dual effect significantly alters carrier dynamics and transition probabilities, promoting radiative recombination while modifying energy band alignment, ultimately improving the optoelectronic performance of the material [35,36]. Therefore, Cu atoms are incorporated into the InP/ZnSe lattice structure, creating intermediate energy states within the InP/ZnSe QDs modifying its bandgap. The Cu^{+} dopants are most likely incorporated into the ZnSe shell or accumulate at the InP/ZnSe interface.

Cu most likely substitutes Zn^{2+} ions in the ZnSe lattice, due to similar ionic radii and oxidation state compatibility. This substitution introduces shallow acceptor states near the valence band edge, which act as radiative centers for NIR emission [37]. These states facilitate radiative transitions from the conduction band to the Cu-induced acceptor level, effectively reducing the emission energy and resulting in the observed redshifted NIR emission. This mechanism is consistent with previously reported behavior in Cu-doped semiconductor nanocrystals, where dopant states act as radiative centers without introducing deep-level non-radiative traps [38]. With the incorporation of Cu dopant, the valence band shifts, and the excited electrons can jump from the conduction band to this newly created Cu state, resulting in significant bandgap tuning from visible to NIR region. The transfer of energy from the host lattice to the dopant states is remarkably efficient, resulting in a prominent emission from the Cu-related states [39–41].

The process described is commonly known as sensitization, where the host material efficiently transfers energy to the dopant, leading to efficient radiance [42]. This also result into the formation of intra-gap states located above the valence band, which leads to a downward shift in the energy of the emitted photons by these QDs. As can be seen in Fig. 3c, the two bands can be observed at 1.9 eV and 1.3 eV. Although the band gap of InP/ZnSe (1.9 eV) QDs is comparatively larger which means more energy is needed to transfer an electron to the conduction band. New energy levels are introduced for the Cu doped QDs, indicated by the dashed lines in the valence and conduction bands, narrowing the bandgap to 1.3 eV. This effectively shows how the electronic structure of InP/ZnSe QDs is altered by copper doping, significantly reducing the band gap energy of the QDs. This reduction in band gap leads to change in optical properties and make them attractive in applications where lower energy emission or absorption is required. We perform TRPL measurements comparing undoped and Cu-doped InP/ZnSe QDs. As (see Figure S3b Supporting Information) that Cu doping leads to a significantly longer PL decay lifetime (up to ~800 ns), confirming slower recombination kinetics associated with dopant-mediated radiative pathways. The undoped QDs exhibit faster decay (~200 ns), indicating stronger non-radiative losses. These results directly validate our claim that Cu doping alters carrier dynamics and enhances radiative recombination efficiency.

2.2. Computational analysis

Density functional theory (DFT) studies were conducted to confirm and further investigate the effect of Cu doping on the bandgap of InP/ZnSe QDs. We performed electronic structure calculations using ab initio DFT with generalized gradient approximation (GGA) as implemented in Vienna Ab-initio Simulation Package (VASP) [36,37]. The projector augmented wave (PAW) method, along with the plane wave basis set, was used for both doped and undoped QDs. Energy convergence test was conducted, the cutoff energy at 500 eV and testing the k-point mesh up to $3 \times 3 \times 1$. The system was simulated using a super cell with a periodic boundary conditions in the x–y plane and a vacuum layer in the z-direction. As illustrated in Fig. 4a and 4b, the spatial distribution of charge carriers (electrons and holes) in undoped quantum dots is inefficient, resulting in suboptimal charge separation. This imbalance can hinder effective charge transfer, increase recombination rates, and ultimately degrade overall device performance by limiting exciton dissociation and transport efficiency.

In contract, Figs. 4c and 4d show that Cu forms stable bonds with the surrounding atoms in InP/ZnSe quantum dots, which helps in stabilizing the overall structure. The Cu dopant in QDs also help to passivate the surface defects, which often act as non-radiative recombination centers that quench photoluminescence and reduce stability.

By passivating these defects, Cu doping enhances the photostability of the QDs [43]. Bader's charge analysis (see Fig. 4c) indicates a uniform charge distribution, with In and Zn atoms transferring charges to P and Se atoms (cyan color represents a transfer of charge while yellow indicates acceptance of charge). After doping, the Cu atom transfers additional charge of approximately 0.23 eV to Se on the surface of the QDs, enhancing charge transfer and improving photostability. This improved charge transfer contributes to more steady and effective current flow in Cu-doped QDs compared to undoped ones [44].

The Projected Density of States (PDOS) for the two distinct quantum dot (QD) materials are computed. Fig. 4e shows undoped QDs where P and Se are the main contributors to the valence band (below the Fermi level), with In also having a certain impact. Se, along with In, dominates the conduction band (above the Fermi level), with Se having a significant influence. The distinct energy gap between these bands indicates that a significant amount of energy is needed to move an electron from the highest occupied states (valence band) to the lowest unoccupied states (conduction band) as shown in Fig. 4b. P and Se contribute more to the valence band than to the conduction band, with Se and In having the most influence.

The addition of Cu doping, as shown in Fig. 4f, modifies the distribution of electronic states, particularly by introducing new energy levels within the band gap of the QDs. These intra-gap states can lead to a reduction in the effective band gap energy, which can shift the photoluminescence (PL) emission to lower energies (redshift) and broaden the

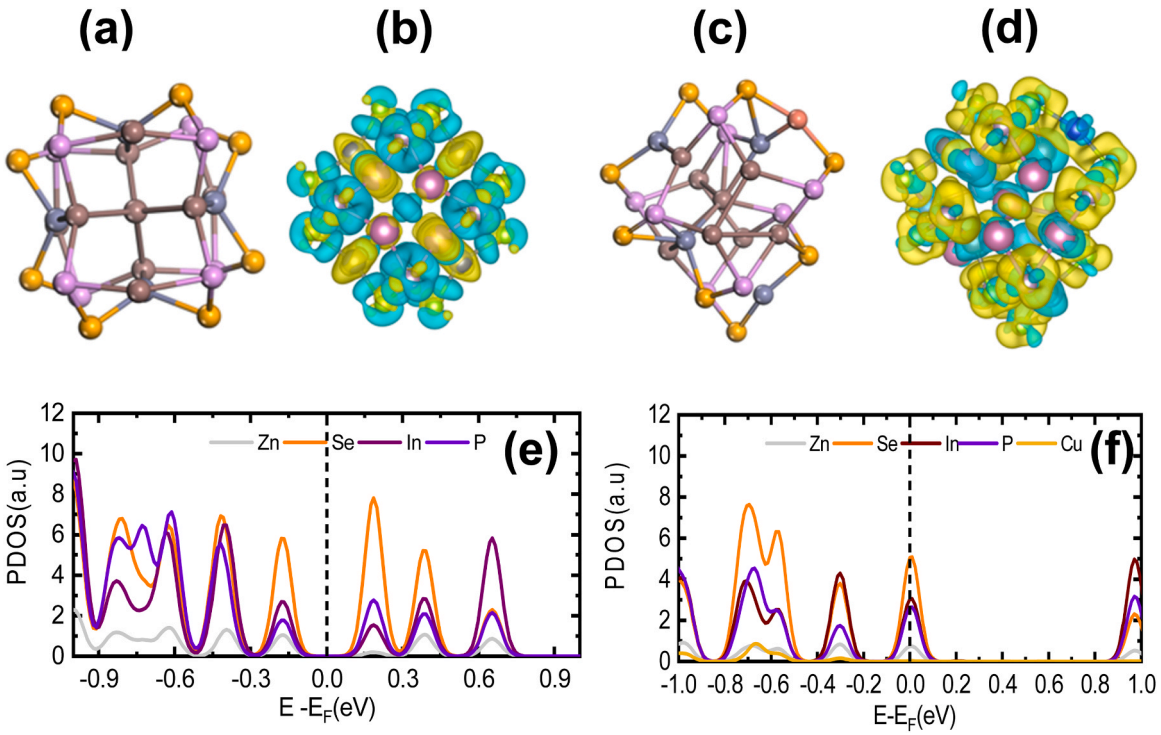

Fig. 4. (a),(c). Electronic structures of undoped and Cu-doped QDs, **(b),(d)** differential charge densities of undoped and Cu-doped QDs, **(e),(f)** Projected density of states of undoped and Cu-doped QDs.

emission spectrum [45,46]. After the Cu-doping in QDs, a notable increase in bond lengths was observed for In-P (2.61–2.63 Å), Zn-Se (2.398–2.432 Å), and Se-P (2.220–2.285 Å). This increase results in a reduced band gap and an enlarged size of the QDs, leading to a diminished quantum confinement effect and consequently longer bond lengths within the quantum dot which is presented in Table 1.

2.3. NIR-QLED characteristics

The final fabricated device is composed of the following structure: ITO/WO_3 (HTL)/ InP/ZnSe:Cu (EML)/ZnMgO (ETL)/Al (cathode), as illustrated in Fig. 5a. To improve the charge balance and understand the mechanism, we fabricated two similar structures with PEDOT:PSS as the HTL and ZnO as the ETL. ITO/PEDOT:PSS (HTL)/InP/ZnSe:Cu (EML)/ZnMgO (ETL)/Al and ITO/WO_3 (HTL)/InP/ZnSe:Cu (EML)/ZnO (ETL)/Al. The energy level diagrams and working mechanisms of the undoped and doped QDs NIR-QLED are illustrated in Figs. 5b and 5c. The tuning of the emissive layer band had a notably large impact on the device performance. Considering the bandgap of InP/ZnSe QDs and the valance band of 5.7 eV, there is a considerable energy offset at the interface for hole injection, which limits the device efficiency. Once the Cu-doped InP/ZnSe QDs are employed, this interface barrier reduces from 5.6 eV to 5.1 eV, as shown in Fig. 5c. This reduction in the energy offset siphoning the holes injecting into the QDs layer, resulting in a significant enhancement in the device efficiency [31]. The high energy barrier also promotes unwanted non-radiative recombination. Charge carriers recombination takes place at this interface resulting in false emission that is not from the QDs. Consequently, a larger external driving voltage is required for charge carriers to overcome the substantial energy barrier, leading to higher operating voltages and inferior device performance. Besides, increased operating voltages can also raise device temperature, which could lead to the Joule thermal effect which shortens the device's lifetime. Zinc oxide (ZnO) is predominantly used as the electron transport layer (ETL) material in the fabrication of InP-based QLEDs. However, the high electron mobility ($\sim 1.2 \times 0^{-3}$ $cm^{-2}S^{-1}V^{-1}$) of ZnO causes the QDs charging, limiting the carriers' recombination within the emissive layer. On the other hand, commonly used hole transport layers (HTLs) such as PEDOT: PSS ($1.0 \times 10^{-4} cm^{-2}V^{-1}S^{-1}$), poly-TPD (-5.4 eV, $1.0 \times 10^{-6} cm^{-2}V^{-1}S^{-1}$), and PVK (-5.8, $1.0 \times 10^{-5} cm^{-2}V^{-1}S^{-1}$) have relatively low hole mobilities [47].

This unequal charge carrier mobilities result in higher electron density than hole density inside the QDs layer, making it an electron-dominant device. Thus, resulting in electroluminance quenching due to the Auger recombination, this may also cause the Joule effect reducing the device lifetime. To overcome this issue, $Zn_{(0.9)}Mg_{(0.1)}O$ was employed as an ETL to facilitate more favorable electron injection into the active layer [48]. Due to its high electron mobility (3.1×10^{-3} $cm^2V^{-1}s^{-1}$) and favorable energy level alignment between ZnMgO (-3.7 eV) and QDs (-3.6 eV), ZnMgO facilitates efficient charge injection into the QD layer. Additionally, its wider bandgap compared to ZnO enhances electron transport while effectively blocking holes, thereby minimizing recombination losses. This property enables ZnMgO to function as an efficient hole-blocking layer (HBL), improving charge carrier recombination and the overall device performance [49]. We use WO_3 as the HTL for the NIR QLED. WO_3 with a hole mobility of about 9.1×10^{-4} $cm^{-2}V^{-1}S^{-1}$ has a deep valence band level that aligns well with the valence band level of InP QDs, thus resulting in efficient hole injection into the QDs active layer. While it

has a wide bandgap and a shallower conduction band level, it helps to block electrons passing through the QDs layer. Therefore, this also acts as an efficient electron-blocking layer (EBL), enhancing recombination [50]. Moreover, the charge transport layers, WO_3 (HTL) and ZnMgO (ETL), exhibit high transparency in the NIR region, minimizing the emitted NIR-photon absorption and maximizing the outcoupling efficiency of the NIR-QLED. The incorporation of these inorganic materials enhances device stability by mitigating degradation pathways commonly associated with organic transport layers. WO_3 facilitates efficient hole injection while ZnMgO ensures balanced electron transport, collectively improving charge recombination and overall device performance, making the NIR-QLED more stable for long-term optoelectronic applications.

To confirm the balanced charge injection, electron-only devices (EOD) and hole-only devices(HOD) were fabricated to investigate the influence of carrier injection on charge transport, and their current density versus voltage (J-V) characteristics were measured. A hole-only device has been designed to only facilitate holes flow, effectively reducing the effect of electron transport. An electron-only device has been designed to facilitate the flow of electrons through the device. The unbalanced charge injection induces undesirable Auger recombination, leakage currents, and Joule heating effect, ultimately degrading overall device performance. An excess of electrons or holes in the EML results in elevated turn-on voltage, compromised device stability, and diminished overall performance. PEDOT:PSS and ZnO are often used as the HTL and ETL in the NIR-QLEDs, respectively [51]. However, we found the Tungsten oxide (WO_3) and Magnesium-doped Zinc Oxide (ZnMgO) show better performances as HTL and ETL in the fabricated NIR-QLED based on InP/ZnSe:Cu QDs. To validate the balanced carrier transport provided by WO_3 (HTL) and ZnMgO (ETL), hole-only devices (HODs) were fabricated using PEDOT and WO_3, as (see Figure S4 a-c Supporting Information). Similarly, electron-only devices (EODs) were fabricated with ZnO and ZnMgO, as shown in Supplementary Figure S4 a-c. The J-V curve comparisons reveal that QLEDs incorporating WO_3 as the HTL and ZnMgO as the ETL demonstrate superior electron-hole transport balance, as depicted in Fig. 6. Consequently, these QLEDs exhibit enhanced NIR emission efficiency. The fabricated device exhibits NIR emission, operating at a turn-on voltage (V_T) of 1.8 V. demonstrating enhanced current density in the Cu-doped structure compared to the undoped counterpart, as illustrated in Fig. 7a. The observed drop in current density shown in Fig. 7a is likely due to carrier trapping and increased non-radiative recombination. This, in trurn reducess the number of free carriers available for conduction. Additionally, Cu-induced scattering may reduce charge carrier mobility and decrease current density.

The optimized NIR-QLED device demonstrates a significantly higher radiance of 62 W sr^{-1} m^{-2} at 0.2 mL Cu doping, as depicted in Fig. 7b. In contrast, devices with 0.1 mL and 0.3 mL Cu doping exhibit lower radiance (see Figure S5a,b, Supporting Information). The device shows a high EQE of 16 %, as shown in Fig. 7c.

We found that Cu-doped devices exhibit higher EQE as compared to undoped structures. Cu-doped InP/ZnSe QDs have a narrow FWHM, which makes them suitable to achieve higher EQE. To achieved high EQE of (~16 %) in our NIR-QLED device by employing WO_3 directly interfacing with InP/ZnSe:Cu quantum dots initially appears contradictory to existing literature, which frequently cites severe emission

Table 1
Change in bond length and charge transfer before and after Cu Doping.

Materials	Bond Length (Å)					Charge transfer (e)			
Quantum Dot	In-P	Zn-Se	In-Zn	Se-P	In	P	Zn	Se	Cu
InP/ZnSe-QD	2.619	2.398	2.709	2.220	0.41	0.318	0.45	−0.345	—
InP/ZnSe:Cu-QD	2.636	2.376–2.432	2.633	2.285	0.55	−0.342	0.44	−0.433	0.23

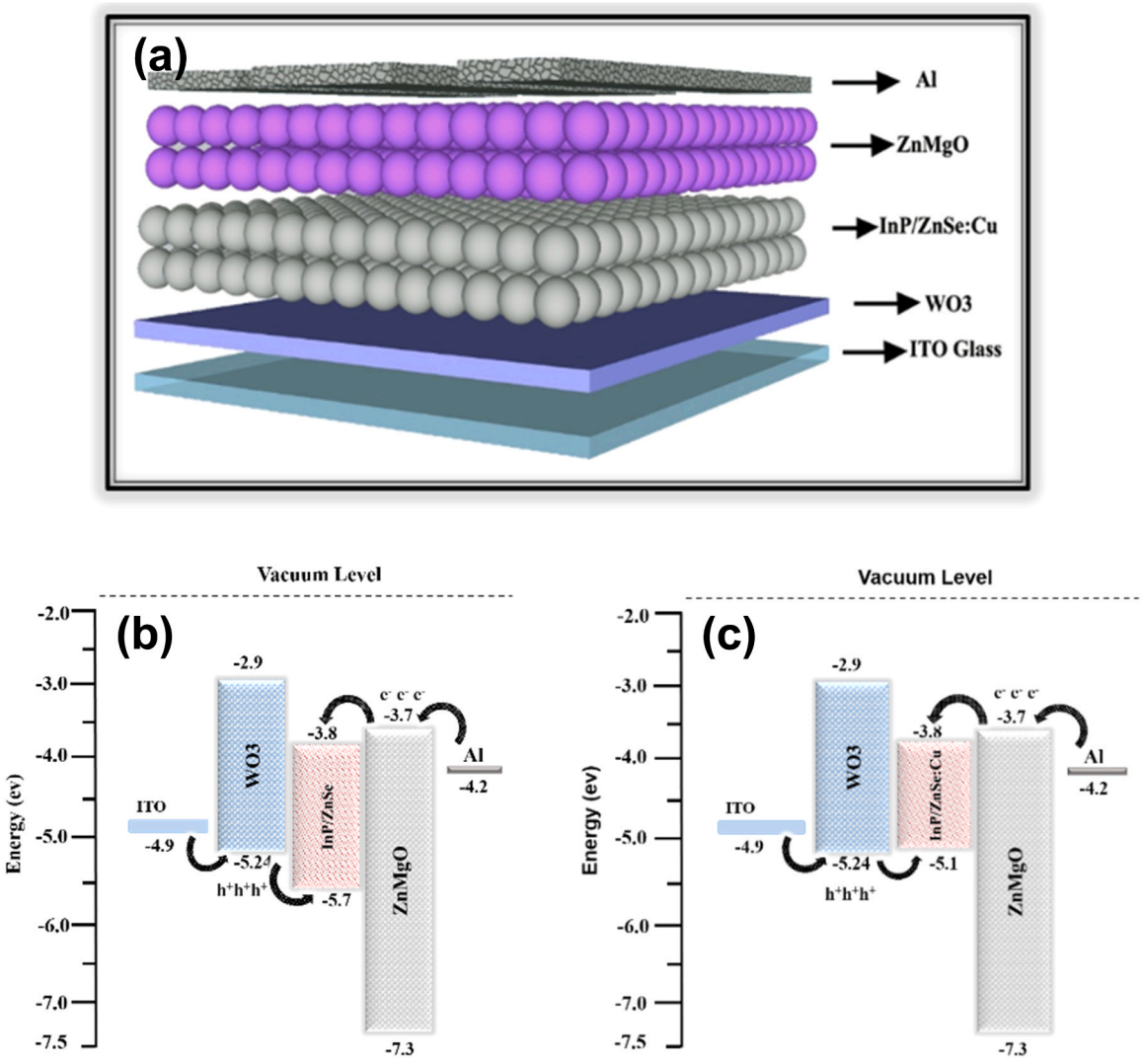

Fig. 5. **(a)** Schematic structure of the fabricated device, **(b)** Energy level diagram of undoped InP/ZnSe QDs **(c)** Energy level diagram of Cu doped InP/ZnSe QDs.

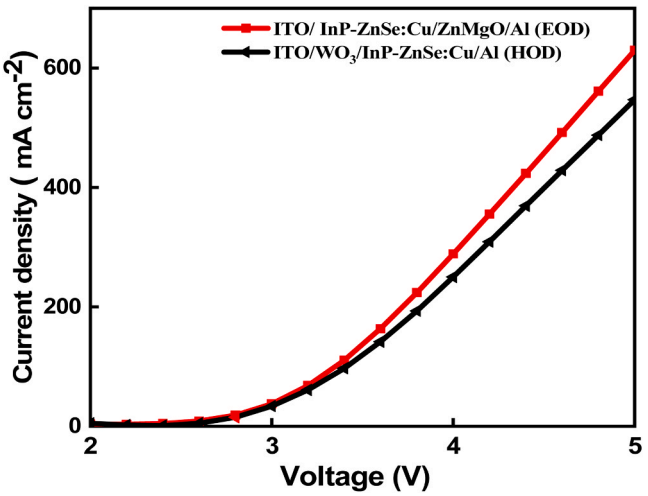

Fig. 6. HOD and EOD of the device.

quenching due to metal oxide-induced non-radiative recombination. We attribute this performance to optimized fabrication parameters, including low-temperature processing and mild annealing of WO_3, resulting in significantly reduced defect densities at the oxide-QD interface. Moreover, rigorous surface passivation of the quantum dots greatly suppressed oxide-induced quenching. We had also calculated our EQE theoretically as shown in in supplementary section which support our experimental results. Our EQE merasurment setup is shown (see Figure S6 Supporting Information).

Furthermore, the desired lifespan of the NIR-QLED devices was calculated which is shown in Fig. 7d. We tested the best-performing NIR-QLEDs over several days at a constant applied voltage to check the stability of the device. As can be seen in Fig. 7d, the devices' radiance stayed noticeably high throughout the stability test. This result strongly indicates that device stability is improved by incorporating inorganic ETL and HTL materials. The enhanced performance is probably attributed to the HTL and ETL materials as they are thermally stable and have lower trap states.

The stability test of the fabricated device, as illustrated in Fig. 7d, was conducted under ambient atmospheric conditions without encapsulation. The device was driven at a constant bias of 3.5 V, exhibiting an initial radiance of 36 W sr^{-1} m^{-2}. Over the first 10 days, radiance remained stable, followed by a gradual decline. The half-lifetime ($T_{1/2}$) was determined to be approximately 40 days, at which point the radiance decayed to 50 % of its initial value. The stability curve is shown in Fig. 7d, depicting the acceptable level of stability of a device. These devices were tested under ambient conditions without any

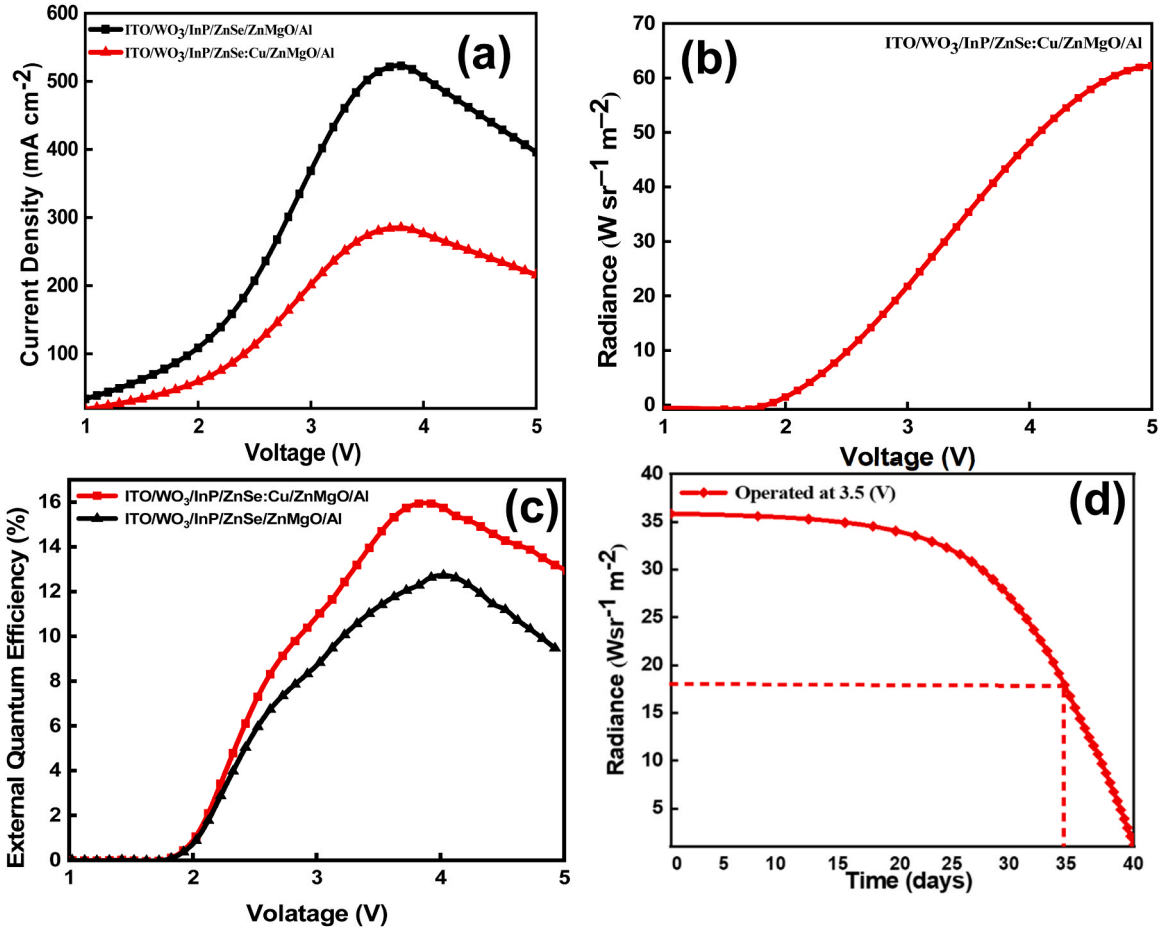

Fig. 7. Device characterization **(a)** Current density vs. voltage, **(b)** Radiance vs. voltage, **(c)** EQE vs. voltage, **(d)** Lifetime of device.

encapsulation making it a good choice for healthcare industry.

Significant progress has been observed by comparing our results on PL emission peak below and above 900 nm, FWHM, radiance, and EQE with data from different studies that investigated different materials, as summarized in Table 2. The comparison shows that our EQE, Radiance, and FWHM are higher than the other reported works where they have utilized Perovskites, Pt-based complexes and other types of QDs. Overall, the work demonstrated in this article presents a new approach to improving the efficiency of NIR-QLEDs. By using suitable material compositions and improved fabrication techniques. We achieved a narrow FWHM, relatively high radiance, and EQE.

2.4. NIR-QLED for non-invasive bioimaging

NIR-QLED effectively enable deep-tissue subcutaneous imaging due to their lower absorption and scattering in biological tissues, facilitating deeper penetration into the human body. Fig. 8a-b show an alternative view of the large-area NIR-QLED in both ON and OFF states. The fabricated device, doped with 0.2 mL of Cu, was employed to illuminate a targeted section of an individual's arm at close proximity. The visibility of subcutaneous blood vessels in Fig. 8c-d provides clear evidence of the device's capacity for non-invasive deep-tissue imaging and illumination. Complementary images as (see Figure S7 Supplementry Material)) display the same arm area illuminated under the 0.1 mL and 0.3 mL Cu-doped NIR-QLEDs, with the 0.2 mL doping yielding superior clarity.

Table 2
Comparison of NIR LEDs efficiencies vs. active material used.

Materials category	Emission Peak (nm)	FWHM (nm)	Radiance (W sr^{-1} m^{-2})	Ext. Quantum Efficiency (EQE)	Lifetime(T_{50})	Ref.
Organic molecules Pt(ii) complexes	930	> 200	41.6	2.1	N/A	[52]
Pb-based QD PbS/PbS QD/ZnO	1400	~200	9	3.8	N/A	[53]
Lead–tin halides FPMAI-$MAPb_{0.6}$ Sn $_{0.4}I3$	917	~100	2.7	5	N/A	[54]
Inorganic tin halides CsSnI3	948	71	226	2.3	39 h @226 W sr^{-1} m^{-2}	[55]
Formamidinium Lead Iodide FAPbI3	799	60	57	20.2	20 h @57 W sr^{-1} m^{-2}	[56]
Colloidal Quantum Dots PbS	1600	150	5	0.5	26068 h @1 W sr^{-1} m^{-2}	[57]
InAs/InP/ZnSe/ZnS	1050	—	581.4	20.5	550 h @50 W sr^{-1} m^{-2}	[58]
InAs/ZnSe	900	134	12	13.3	30 min@0.1 W sr^{-1} m^{-2}	[59]
In(Zn)As–In(Zn)P–GaP–ZnS	1006	—	——	13.3	———	[60]
Our work						
Cd Free Quantum Dots InP/ZnSe:Cu	924	81	62	16	40 days @36 W sr^{-1} m^{-2}	

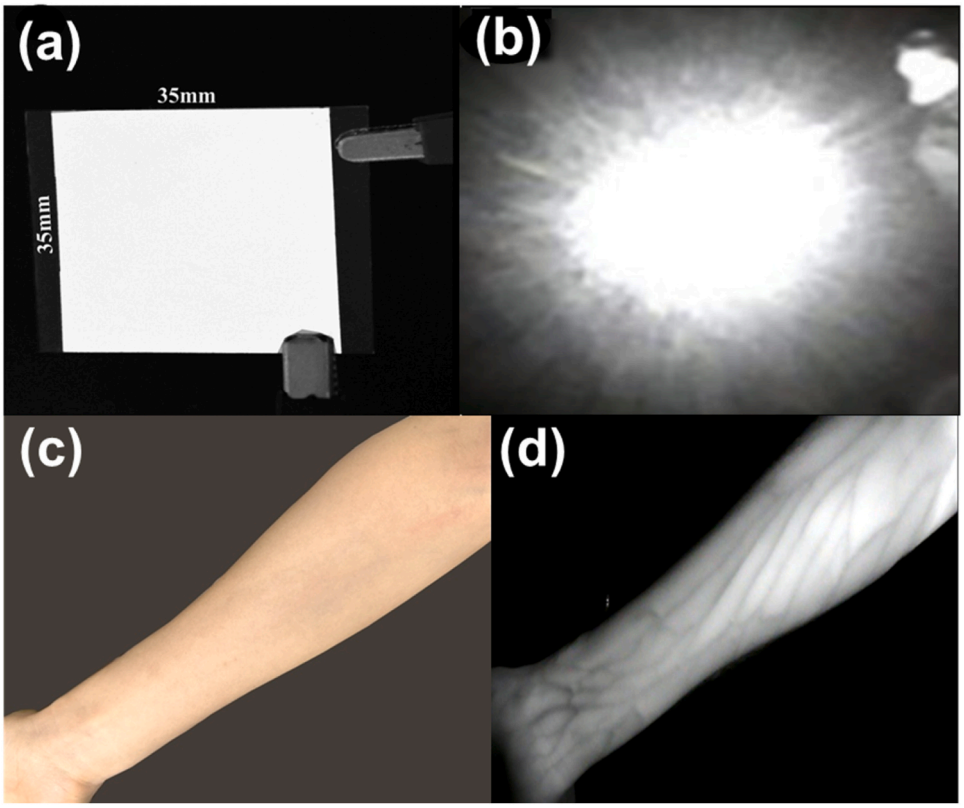

Fig. 8. **(a)** Device at OFF state, **(b)** device at ON state, **(c)** Human hand at OFF state of the device, **(d)** human hand at ON state of the device.

This study demonstrates the successful development of NIR-QLEDs characterized by high uniformity and impressive operational performance. Furthermore, these devices show promise for applications in monitoring blood volume and heart rate using photoplethysmography. The demonstrated effectiveness in deep-tissue imaging highlights their potential in the emerging market for wearable medical devices. The increasing demand for power-efficient, flexible, and large-area devices underscores their utility in various health applications, including detecting blood clots, monitoring vascular obstructions, evaluating muscular performance in athletes and disabled individuals, and diagnosing malignant tumors in tissues.

3. Conclusion

NIR-QLED technology has significant potential in blood vessel imaging due to its enhanced depth penetration and reduced scattering compared to visible light, enabling more precise visualization of the vascular network. This capability is critical for diagnosing and treating various vascular conditions. Experimental results demonstrate that Cu doping significantly enhances the performance of the InP/ZnSe device, emitting NIR light at 924 nm with a narrow FWHM of 81 nm. The device exhibits a low turn-on voltage of 1.8 V, achieves a maximum EQE of 16 %, and delivers a peak radiance of 62 W sr^{-1} m^{-2}. Additionally, it maintains good stability, with a half-life of 960 h of continuous operation without encapsulation. Ongoing research and innovations are expected to enhance the capabilities of NIR-QLED bioimaging, making it an increasingly valuable tool for healthcare professionals and researchers. Improved accuracy and sensitivity in visualizing blood vessels, detecting blood clots, and identifying malignancies offer significant potential for advancing patient care and deepening our understanding of these critical aspects of human health.

Furthermore, NIR-QLED can be employed in angiography and tumor imaging, a critical component of surgical interventions that enable surgeons to navigate complex arterial networks with precision. Looking ahead, the continuous evolution of NIR-QLED technology holds significant potential. Ongoing research and innovations are anticipated to enhance the capabilities of NIR-QLED bioimaging, making it an increasingly valuable tool for healthcare professionals and researchers. Improved accuracy and sensitivity in visualizing blood vessels, detecting blood clots, and identifying malignancies offer significant potential for advancing patient care and deepening our understanding of these critical aspects of human health.

4. Experimental section

Materials: O-Phenylenediamine, benzenesulfonyl chloride, potassium carbonate, sulfuric acid, dichloromethane (DCM), indium(III) chloride, zinc(II) chloride, benzyle chloride, zinc stearate (technical grade), trioctylphosphine (TOP), and oleylamine (OLAm), sodium borohydride ($NaBH_4$), acetic acid, toluene, tiethylamine, diethylamine, and phosphorus tribromide were purchased from Sigma-Aldrich. Selenium powder and copper stearate were purchased from Xi'an Chemicals and Chloroform was purchased from Aladdin.

4.1. Synthesis core/shell quantum dots

4.1.1. Preparation of diamines

The synthesis of the amine involves a three-step process, adopted from previously reported procedure with several modifications, as detailed below [61,62].

Step 1: 10 g of benzene sulfonylchloride was slowly added to a solution of 2 g of O-Phenylenediamine in 30 mL of DCM. The resulting solution was stirred for 4 h at room temperature. Progress of the reaction was monitored with thin-layer chromatography (TLC) using a 1:1 vol ratio of n-hexane and ethyl acetate. After the completion of the reaction, DCM was evaporated using a Rotary evaporator. Then wash the resulting powder with DI water several times. Keep the resulting powder in an air-free bottle.

Step 2: 4.4 g of K_2CO_3 was added to the solution of 3 g of the amine dissolved in 20 mL of acetonitrile and stirred at room temperature. After 1 h, the temperature of the solution was reduced to 0 °C and 6.32 mL of benzyl chloride was slowly added to the solution and refluxed for about 1–2 h. The solution obtained was then filtered using a Celite pad. Furthermore, the filtrate was dissolved in 50 mL of CH_2Cl_2 and rinsed twice with about 50 mL of water. The organic component was obtained using sodium sulphate solution to achieve N,N'-(1,2-phenylene)bis(N-benzyl-4-methylbenzenesulfonamide) and the resulting product was stored in an airtight container due to its sensitivity to atmosphere.

Step 3: 2.9 g of *N,N'*-(1,2-phenylene)bis(N-benzyl-4-methylbenzenesulfonamide) was dissolved in 4 mL of conc. sulfuric acid and the mixture was heated at 85 °C for 4 h. The reaction was monitored with TLC technique, and the resulting product was transferred into a beaker containing 50 mL of ice. 50 mL solution of 4 M aqueous sodium hydroxide was slowly added to the beaker and the product was extracted using 100 mL of CH_2Cl_2 and then the resultant solution was rinsed with 4 M NaOH solution before drying with sodium sulphate. After evaporation, a brown oily product was obtained, which was identified as crude N^1,N^2-dibenzylbenzene-1,2-diamine. The crude product is unstable in air and light and hence it was immediately utilized for the subsequent procedure.

4.1.2. Preparation of aminophosphines

The synthesis of aminophosphines was carried out according to the previously reported procedure with several modifications. 3 g of the synthesized diamine, 5.25 mL of trimethylamine, and 50 mL of dehydrated toluene were added to a 100 mL Schlenk line and the mixture was cooled in an ice bath. After about 10 min PBr_3 (2.36 mL) was dropwise added to the solution. The addition of PBr_3 resulted in the crystallization of triethylammonium chloride, which appeared as a white substance and the mixture was then stirred for 30 min and filtered under vacuum. This process was followed with the addition of triethylamine (2.34 mL) and diethylamide (1.68 mL), and the solution was then agitated for 3 h in an argon-filled glove box. This process yielded the desired aminophosphine compound. The resulting yellowish oil, 1,3-dibenzyl-*N,N*-diethyl-1,3-dihydro-2H-benzo[*d*][1–3]diazaphosphol-2-amine, was promptly transferred into a hermetically sealed container for subsequent utilization.

4.1.3. Preparation of InP quantum dots core

Synthesis of the nanoparticles was conducted under an inert environment using the Schlenk line setup. A 50 mL three-necked round bottom flask was used that contained a mixture of $InCl_3$ (99.5 mg), $ZnCl_2$ (307 mg), and OLAm (5 mL). The mixture was heated at 120 °C under the vacuum condition of 0.5 Torr, facilitating the elimination of any oxygen and water contaminants. Subsequently, the flask was refilled with neon gas, and the temperature was elevated to 180 °C. A solution of aminophosphines (0.614 mg) in OLAm (x mL) was promptly injected into the reaction flask, and the reaction was allowed to progress for 30 min. Thereafter, the reaction temperature was subsequently decreased expeditiously by submerging the flask in cold water. Excess ethanol was added to the flask to precipitate the nanoparticles and then centrifuged to get the nanoparticles separated from the solvent. Three cycles of dissolution and re-precipitation were conducted using absolute ethanol:chloroform mixture (v/v, 1/3) to achieve the purified mixture. The QDs were dispersed in $CHCl_3$ and stored in a refrigerator.

4.2. Synthesis of core/shell indium phosphide/zinc selenide quantum dots

The same procedure was followed as presented in 2.4, but before the termination of the reaction, a solution of 0.8 g of selenium in 10 mL of OLAm was gradually added to InP core for 2 h. After the addition of the selenium, the solution temperature was increased to 200 °C, followed by the addition of 1.6 g of zinc stearate in 0.8 mL of OLAm solution. The reaction was continued for 20 min and then about 1.5 mL of the selenium (2.24 M) solution was dropwise added to the mixture while the temperature of the reaction was maintained at 200 °C. Thereafter, the temperature was increased to 260 °C and at this stage, 0.8 mL of the zinc stearate solution was added and the reaction was allowed to proceed for about 1.7 h. After the reaction was completed, the flask was allowed to cool to 65 °C and ethanol was added to allow the quantum dots to precipitate at the bottom. For purification, we followed the same process as presented in 2.4.

4.3. Synthesis of InP/ZnSe:Cu quantum dots

Cu-doped InP/ZnSe QDs were synthesized according to the previously reported method [63]. Typically, 1 mL of Cu-OLAm (0.6 g of copper stearate in 10 mL of OLAm) added to InP/ZnSe QDs solution at 240 °C with different ratios of Cu-OLAm and each reaction was allowed to continue for 1.5 h. The concentration that yielded the most optimized outcome was selected and the reaction with Cu-OLAm was conducted using the same quantities as reported in previous studies i.e. 0.1, 0.2, and 0.3 mL. The reaction temperature was maintained at 240 °C for 1.5 h to synthesize InP/ZnSe:Cu quantum dots in various sizes, which were then purified by using a specified ratio of anhydrous acetone and hexane. The QD samples synthesized were designated as InP/ZnSe: Cu (0.1 mL), InP/ZnSe:Cu(0.2 mL), and InP/ZnSe:Cu(0.3 mL), indicating the concentration of the dopant.

4.4. Characterizations

The thickness of the layer was measured using field emission electron microscopy (FESEM, FEI Quanta 200). X-ray diffraction (XRD) data was acquired with Smart Lab 3 diffractometer. High-resolution transmission electron microscopy (HR-TEM) images were obtained using FEI Tecnai G20 instrument. The current density versus voltage characteristics were measured using the Keithley 2450 source-measure unit. Voltage was varied from 0 to 5 V with increments of 0.21 V and a delay of 1 s. Photoluminescence and UV–vis absorbance spectra of the samples were measured on calibrated Ocean Optics Flame-T and Flame-NIR spectrometer, respectively. For measuring the external quantum efficiency (EQE), Lambertian emission profile was employed. Photographs of the light-emitting device were captured in a dark room using a Canon 200D DSLR camera that was customized for infrared (IR) imaging. The quantum yield (QY) was determined by using the EDINBURGD (FS5) system. All measurements were conducted in a natural environment.

4.5. Device fabrication

A large-area, 35 mm × 35 mm, device was fabricated. The ITO substrate was washed with detergent and subjected to a 15-minute cleaning process in an ultrasonic machine using DI water, acetone, and IPA as the solvents stepwise. UV treatment was carried out for 30 min, and a solution of WO_3 HTL (10 mg mL^{-1} in ethanol) was employed to fabricate a hole transport layer. The spin-coating technique was utilized for 30 s at a rotational speed of 5000 rpm to uniformly distribute the solution on the substrate. Following the spin-coating process, the substrate was subjected to a baking process at a temperature of 120 °C for 30 min. The Cu-doped InP/ZnSe quantum dot (QD) solution, with a concentration of 10 mg mL^{-1} in octane, was prepared by spin-coating at 1500 rpm for 30 s. Subsequently, the QD solution was annealed at 120 °C for 10 min. The electron transport layers (ETLs), were prepared by spin-coating using the ZnMgO solution with a concentration of 10 mg mL^{-1} for 30 s at a rotational speed of 3000 rpm, and the coated layers were annealed at 60 °C for 10 min. Following the deposition of the ZnMgO layer, the Al electrodes were then deposited using the thermal deposition method under a base pressure of approximately 4×10^{-4} Pascal (Pa) as shown in Figure S1, Supplementry Material.

CRediT authorship contribution statement

Wei Lei: Supervision. **Sajid Hussain:** Formal analysis. **Rai Muhammad Dawood Sultan:** Writing – original draft. **Jianming Zhou:** Data curation. **Byung Seong Bae:** Formal analysis. **Qasim Khan:** Supervision. **Damian C. Onwudiwe:** Formal analysis. **Nasrud Din:** Writing – review & editing, Writing – original draft, Visualization, Resources, Methodology, Investigation, Formal analysis, Data curation, Conceptualization. **Zaman Ashraf:** Methodology. **Fawad Saeed:** Formal analysis. **Premkumar Sellan:** Visualization. **Qing Li:** Data curation. **Zhiwei Zhao:** Formal analysis. **Zhuoya Zhu:** Formal analysis. **Zhang Yuyi:** Conceptualization.

Funding

This work is financially supported by the National Key Research and Development Program of China (2022YFE0139100), the National Natural Science Foundation Project of China (62175028), the International cooperative research project of Jiangsu province (BZ2022008), Program 111_2.0 in China (BP0719013), Leading Technology of Jiangsu Basic Research Plan (BK20192003).

Declaration of Competing Interest

The authors declare the following financial interests/personal relationships which may be considered as potential competing interests: LeiWei reports financial support was provided by National Key Research and Development Program of China. Lei Wei reports was provided by National Natural Science Foundation Project of China. Lei Wei reports was provided by the International cooperative research project of Jiangsu province. If there are other authors, they declare that they have no known competing financial interests or personal relationships that could have appeared to influence the work reported in this paper.

Acknowledgements

Not applicable

Appendix A. Supporting information

Supplementary data associated with this article can be found in the online version at doi:10.1016/j.nanoen.2025.111316.

Data availability

Data will be made available on request.

References

[1] V.L. Colvin, M.C. Schlamp, A.P. Alivisatos, Light-emitting diodes made from cadmium selenide nanocrystals and a semiconducting polymer, Nature 370 (6488) (1994) 354–357.
[2] H. Shen, et al., Visible quantum dot light-emitting diodes with simultaneous high brightness and efficiency, Nat. Photonics 13 (3) (2019) 192–197.
[3] Y. Shirasaki, et al., Emergence of colloidal quantum-dot light-emitting technologies, Nat. Photonics 7 (1) (2013) 13–23.
[4] Z. Zhang, et al., High-performance, solution-processed, and insulating-layer-free light-emitting diodes based on colloidal quantum dots, Adv. Mater. 30 (28) (2018) 1801387.
[5] K.R. Choudhury, D.W. Song, F. So, Efficient solution-processed hybrid polymer–nanocrystal near infrared light-emitting devices, Org. Electron. 11 (1) (2010) 23–28.
[6] J. Song, et al., Over 30% external quantum efficiency light-emitting diodes by engineering quantum dot-assisted energy level match for hole transport layer, Adv. Funct. Mater. 29 (33) (2019) 1808377.
[7] B. Chen, D. Li, F. Wang, InP quantum dots: synthesis and lighting applications, Small 16 (32) (2020) 2002454.
[8] C. Bi, et al., Perovskite quantum dots with ultralow trap density by acid etching-driven ligand exchange for high luminance and stable pure-blue light-emitting diodes, Adv. Mater. 33 (15) (2021) 2006722.
[9] A.P. Alivisatos, Perspectives on the physical chemistry of semiconductor nanocrystals, J. Phys. Chem. 100 (31) (1996) 13226–13239.
[10] A.P. Alivisatos, Semiconductor clusters, nanocrystals, and quantum dots, science 271 (5251) (1996) 933–937.
[11] M. Chen, et al., High performance inkjet-printed QLEDs with 18.3% EQE: improving interfacial contact by novel halogen-free binary solvent system, Nano Res. (2021) 1–7.
[12] Z. Yao, et al., High brightness and stability pure-blue perovskite light-emitting diodes based on a novel structural quantum-dot film, Nano Energy 95 (2022) 106974.
[13] Z. Chen, et al., Color revolution: prospects and challenges of quantum-dot light-emitting diode display technologies, Small Methods 8 (2) (2024) 2300359.
[14] L.J. Lim, X. Zhao, Z.K. Tan, Non-Toxic CuInS2/ZnS colloidal quantum dots for near-infrared light-emitting diodes, Adv. Mater. 35 (28) (2023) 2301887.
[15] S. Zhao, et al., Developing near-infrared quantum-dot light-emitting diodes to mimic synaptic plasticity, Sci. China Mater. 62 (10) (2019) 1470–1478.
[16] D. Battaglia, X. Peng, Formation of high quality InP and InAs nanocrystals in a noncoordinating solvent, Nano Lett. 2 (9) (2002) 1027–1030.
[17] S. Wang, et al., Development and challenges of indium phosphide-based quantum-dot light-emitting diodes, J. Photochem. Photobiol. C Photochem. Rev. 55 (2023) 100588.
[18] C.B. Murray, et al., Colloidal synthesis of nanocrystals and nanocrystal superlattices, IBM J. Res. Dev. 45 (1) (2001) 47–56.
[19] L. Cui, X.-P. He, G.-R. Chen, Recent progress in quantum dot based sensors, Rsc Adv. 5 (34) (2015) 26644–26653.
[20] W.W. Yu, et al., Preparation and characterization of monodisperse PbSe semiconductor nanocrystals in a noncoordinating solvent, Chem. Mater. 16 (17) (2004) 3318–3322.
[21] J.M. Pietryga, et al., Pushing the band gap envelope: mid-infrared emitting colloidal PbSe quantum dots, J. Am. Chem. Soc. 126 (38) (2004) 11752–11753.
[22] W. Hu, et al., Near-infrared quantum dot light emitting diodes employing electron transport nanocrystals in a layered architecture, Nanotechnology 23 (37) (2012) 375202.
[23] J.S. Steckel, et al., 1.3 μm to 1.55 μm tunable electroluminescence from PbSe quantum dots embedded within an organic device, Adv. Mater. 15 (21) (2003) 1862–1866.
[24] N. Tessler, et al., Efficient near-infrared polymer nanocrystal light-emitting diodes, Science 295 (5559) (2002) 1506–1508.
[25] B.L. Wehrenberg, C. Wang, P. Guyot-Sionnest, Interband and intraband optical studies of PbSe colloidal quantum dots, J. Phys. Chem. B 106 (41) (2002) 10634–10640.
[26] F.W. Wise, Lead salt quantum dots: the limit of strong quantum confinement, Acc. Chem. Res. 33 (11) (2000) 773–780.
[27] J. Sun, D. Choi, Stachnik, AC Bartnik, B.-R. Hyun, GG Malliaras, T. Hanrath, and FW Wise, Nat. Nanotechnol. 7 (6) (2012) 369–373.
[28] G.J. Supran, et al., High-performance shortwave-infrared light-emitting devices using core-shell (PbS-CdS) colloidal quantum dots, Adv. Mater. (Deerfield Beach Fla.) 27 (8) (2015) 1437–1442.
[29] L. Yan, et al., Tunable near-infrared luminescence of PbSe quantum dots for multigas analysis, Anal. Chem. 86 (22) (2014) 11312–11318.
[30] D. Meng, et al., Near-infrared materials: the turning point of organic photovoltaics, Adv. Mater. 34 (10) (2022) 2107330.
[31] D. Jung, et al., Strain-graded quantum dots with spectrally pure, stable and polarized emission, Nat. Commun. 15 (1) (2024) 5561.
[32] N. Park, et al., Tuning the interfacial stoichiometry of InP core and InP/ZnSe core/shell quantum dots, J. Chem. Phys. 155 (8) (2021).
[33] S. Savchenko, A. Vokhmintsev, I. Weinstein, Exciton–phonon interactions and temperature behavior of optical spectra in core/shell InP/ZnS Quantum Dots, Core/Shell Quantum Dots Synthesis Properties Devices (2020) 165–196.
[34] B. Choudhury, M. Dey, A. Choudhury, Shallow and deep trap emission and luminescence quenching of TiO 2 nanoparticles on Cu doping, Appl. Nanosci. 4 (2014) 499–506.
[35] C. Li, P. Wu, Cu-doped quantum dots: a new class of near-infrared emitting fluorophores for bioanalysis and bioimaging, Luminescence 34 (8) (2019) 782–789.
[36] H. Zhao, et al., Role of copper doping in heavy metal-free InP/ZnSe core/shell quantum dots for highly efficient and stable photoelectrochemical cell, Adv. Energy Mater. 11 (31) (2021) 2101230.
[37] G. Murugadoss, Luminescence properties of co-doped ZnS: Ni, Mn and ZnS: Cu, Cd nanoparticles, J. Lumin. 132 (8) (2012) 2043–2048.
[38] A. Fuhr, et al., Spectroscopic and magneto-optical signatures of Cu1+ and Cu2+ defects in copper indium sulfide quantum dots, ACS nano 14 (2) (2020) 2212–2223.
[39] Z. Ma, et al., Recent advances and opportunities of eco-friendly ternary copper halides: a new superstar in optoelectronic applications, Adv. Mater. 35 (44) (2023) 2300731.
[40] P. Sheng, et al., Synthesis of near-infrared zinc-induced manganese-doped Cu-In-Se quantum dots and their photoluminescence mechanism, J. Alloy. Compd. 947 (2023) 169642.
[41] Y. You, et al., Eco-friendly colloidal quantum dot-based luminescent solar concentrators, Adv. Sci. 6 (9) (2019) 1801967.
[42] X. Tang, et al., Highly efficient luminescence from space-confined charge-transfer emitters, Nat. Mater. 19 (12) (2020) 1332–1338.
[43] H. Guo, et al., Boosting photoelectrochemical hydrogen generation on Cu-doped AgIn 5 S 8/ZnS colloidal quantum dot sensitized photoanodes via shell-layer homojunction defect passivation, J. Mater. Chem. A 8 (46) (2020) 24655–24663.

[44] B. Roy, et al., Cu-doping induced phase transformation in CsPbI3 nanocrystals with enhanced structural stability and photoluminescence quantum yield, Chem. Mater. 35 (4) (2023) 1601–1609.
[45] F.W. Eagle, et al., Enhanced charge transfer from coinage metal doped InP quantum dots, ACS Nanosci. Au 3 (6) (2023) 451–461.
[46] J. Kim, et al., Highly luminescent near-infrared Cu-doped InP quantum dots with a Zn–Cu–In–S/ZnS double shell scheme, J. Mater. Chem. C. 9 (12) (2021) 4330–4337.
[47] S. Hussain, et al., Engineering architecture of quantum dot-based light-emitting diode for high device performance with double-sided emission fabricated by nonvacuum technique, ACS Appl. Electron. Mater. 2 (8) (2020) 2383–2389.
[48] C.-Y. Han, et al., Development of colloidal quantum dots for electrically driven light-emitting devices, J. Korean Ceram. Soc. 54 (6) (2017) 449–469.
[49] X. Jin, et al., Balancing the electron and hole transfer for efficient quantum dot light-emitting diodes by employing a versatile organic electron-blocking layer, ACS Appl. Mater. Interfaces 10 (18) (2018) 15803–15811.
[50] S. Rhee, et al., Steering interface dipoles for bright and efficient all-inorganic quantum dot based light-emitting diodes, ACS nano 15 (12) (2021) 20332–20340.
[51] X. Dai, et al., Quantum-dot light-emitting diodes for large-area displays: towards the dawn of commercialization, Adv. Mater. 29 (14) (2017) 1607022.
[52] Y.-C. Wei, et al., Overcoming the energy gap law in near-infrared OLEDs by exciton–vibration decoupling, Nat. Photonics 14 (9) (2020) 570–577.
[53] X. Gong, et al., Highly efficient quantum dot near-infrared light-emitting diodes, Nat. Photonics 10 (4) (2016) 253–257.
[54] W. Qiu, et al., Mixed lead–tin halide perovskites for efficient and wavelength-tunable near-infrared light-emitting diodes, Adv. Mater. 31 (3) (2019) 1806105.
[55] F. Yuan, et al., Bright and stable near-infrared lead-free perovskite light-emitting diodes, Nat. Photonics 18 (2) (2024) 170–176.
[56] X. Zhao, Z.-K. Tan, Large-area near-infrared perovskite light-emitting diodes, Nat. Photonics 14 (4) (2020) 215–218.
[57] S. Pradhan, et al., Highly efficient, bright, and stable colloidal quantum dot short-wave infrared light-emitting diodes, Adv. Funct. Mater. 30 (39) (2020) 2004445.
[58] B. Li, et al., Efficient and stable near-infrared InAs quantum dot light-emitting diodes, Nat. Commun. 16 (1) (2025) 2450.
[59] H. Roshan, et al., Near infrared light-emitting diodes based on colloidal InAs/ZnSe core/thick-shell quantum dots, Adv. Sci. 11 (23) (2024) 2400734.
[60] X. Zhao, et al., Efficient short-wave infrared light-emitting diodes based on heavy-metal-free quantum dots, Adv. Mater. 34 (45) (2022) 2206409..
[61] D. Nasrud, et al., Solution Processed Light Emitting Diode Based on InP Quantum Dots with Hybrid Emissive Layer. Journal of Physics: Conference Series, IOP Publishing, 2023.
[62] R. Valleix, et al., Size-controlled indium phosphide quantum dots for bright and tunable light emission by simple hindered diamine addition, ACS Appl. Nano Mater. 4 (10) (2021) 11105–11114.
[63] H.-J. Kim, et al., Emission enhancement of Cu-doped InP quantum dots through double shelling scheme, Materials 12 (14) (2019) 2267.